processes

MDPI

Article

Research on Real-Time Prediction Method of Photovoltaic Power Time Series Utilizing Improved Grey Wolf Optimization and Long Short-Term Memory Neural Network

Xinyi Lu *, Yan Guan, Junyu Liu, Wenye Yang, Jiayin Sun and Jing Dai

Electricity Intensive Control Department State Grid Liaoning Marketing Service Center, Shenyang 110000, China; guanyan@163.com (Y.G.); liujunyu@163.com (J.L.); yangwenye1993@163.com (W.Y.); sunjiayin1987@163.com (J.S.); daiqing@163.com (J.D.)

* Correspondence: xinyi_lu1990@163.com

Abstract: This paper proposes a novel method for the real-time prediction of photovoltaic (PV) power output by integrating phase space reconstruction (PSR), improved grey wolf optimization (GWO), and long short-term memory (LSTM) neural networks. The proposed method consists of three main steps. First, historical data are denoised and features are extracted using singular spectrum analysis (SSA) and complete ensemble empirical mode decomposition with adaptive noise (CEEMDAN). Second, improved grey wolf optimization (GWO) is employed to optimize the key parameters of phase space reconstruction (PSR) and long short-term memory (LSTM) neural networks. Third, real-time predictions are made using LSTM neural networks, with dynamic updates of training data and model parameters. Experimental results demonstrate that the proposed method has significant advantages in both prediction accuracy and speed. Specifically, the proposed method achieves a mean absolute percentage error (MAPE) of 3.45%, significantly outperforming traditional machine learning models and other neural network-based approaches. Compared with seven alternative methods, our method improves prediction accuracy by 15% to 25% and computational speed by 20% to 30%. Additionally, the proposed method exhibits excellent prediction stability and adaptability, effectively handling the nonlinear and chaotic characteristics of PV power.

Keywords: photovoltaic; power prediction; improved grey wolf optimization; complete ensemble empirical mode decomposition with adaptive noise; long short-term memory neural network; online model

Citation: Lu, X.; Guan, Y.; Liu, J.; Yang, W.; Sun, J.; Dai, J. Research on Real-Time Prediction Method of Photovoltaic Power Time Series Utilizing Improved Grey Wolf Optimization and Long Short-Term Memory Neural Network. *Processes* **2024**, *12*, 1578. https://doi.org/10.3390/pr12081578

Academic Editors: Yifei Tong, Fengque Pei and Yuliya Sergeevna Ivanova

Received: 11 June 2024
Revised: 16 July 2024
Accepted: 22 July 2024
Published: 28 July 2024

1. Introduction

Because it is affected by meteorology, geographic location and other factors, the output of photovoltaic (PV) power generation possesses a strong intermittence and volatility. When a substantial portion of PV-generated electricity is integrated into the grid, these characteristics can significantly impact grid stability [1]. An accurate prediction of PV power output can provide the smooth operation of a power grid. Additionally, in the context of electricity market regulation, the dynamic nature of PV power generation introduces challenges for market operators in maintaining grid balance and stability. Therefore, developing effective PV power prediction models that account for intermittency and fluctuations is critical for informing decision-making processes within the electricity market regulation framework.

The prediction time scales for the generation of PV can be categorized into long term, medium term, short term, and ultra-short term. At the present time, the methods for PV power prediction can be separated into physically based and data-driven methods according to the modeling principles [2,3]. Among these, physical methods are usually based on the principle of investigating the generation of electricity from PV cells. For the physical method, the PV output values are directly calculated via physical modeling using installation parameters for equipment and numerical weather prediction (NWP) data [4,5]. However, the

complexity of physical modeling necessitates detailed NWP data and equipment parameters, rendering these approaches susceptible to environmental fluctuations.

In contrast, the data-driven methods construct regression models between data characteristic values and prediction targets by combining statistical theory as well as machine learning [6–8]. These methods can be additionally classified into models that consider multiple variables and those that focus on a single variable [9]. The multivariate model establishes a regression mapping relationship with the target value by combining meteorological parameters, including temperature, irradiance, wind speed, and power data [10]. Although the inclusion of multiple variables enhances predictive accuracy, it also exacerbates model complexity, thereby potentially compromising stability and robustness, particularly under varying weather conditions [11]. Conversely, single-variate models exploit historical PV power data to elucidate fundamental PV power laws, offering simplicity in acquisition and modeling. Such models demonstrate adaptability and are especially effective for PV power predictions on ultra-short- and short-term time scales [12,13].

The output of PV power generation fluctuates over time and exhibits chaotic behavior. The chaotic theory-based method of PV power prediction can improve prediction accuracy and reliability [14]. The conventional idea is to combine signal decomposition algorithms with phase space reconstruction theory. The uncertainty information in the power data is transformed into the information of predictability and regularity. All of the typical signal decomposition algorithms contain either wavelet decomposition (WD), empirical mode decomposition (EMD), ensemble empirical mode decomposition (EEMD), or complete ensemble empirical mode decomposition with adaptive noise (CEEMDAN) [15–17]. Meanwhile, the methods based on the analysis theory of chaotic characteristic include singular spectrum analysis (SSA) and phase space reconstruction (PSR). The prediction is then based on a neural network model with strong nonlinear fitting ability. Neural network algorithms with a superior performance in prediction include support vector machine (SVM) [18], kernel-based extreme learning machine (KELM) [19], and long-short-term memory (LSTM) [20]. Therefore, the chaotic properties of PV power have been analyzed in numerous studies and the prediction models have been improved by combining various methods to achieve higher prediction accuracies. Wang et al. proposed an ultra-short-term PV prediction method combining phase space reconstruction, gray wolf algorithm, and an enhanced emotional neural network. The proposed method overcomes the adverse effects of random changes under highly volatile weather conditions [21]. Zhang et al. proposed a method based on affinity propagation clustering, complete ensemble empirical mode decomposition with an adaptive noise algorithm and bi-directional long and short-term memory network for ultra-short-term PV power prediction [22]. The proposed method can achieve accurate PV power predictions for different weather types. Gu et al. proposed a prediction method (FCM-WOA-LSSVM) with the utilization of the fuzzy C-means, whale optimization algorithm, and least squares support vector machine [23]. The uncertainty of power data is recognized by FCM. The optimal parameters of LSSVM are obtained using WOA for optimal searching. Spyros et al. [24] utilized optimized Bayesian neural networks (BNN), support vector machine regression (SVR), and regression tree (RT) models, to forecast daily PV power. The prediction accuracy of the designed models is shown in Table 1. The above methods each utilize offline historical data to train prediction models. The unknown PV power is predicted based on the offline trained model. Thus, this prediction idea can be referred to as an offline prediction model [25,26].

The offline prediction methods enable researchers to investigate the impact of different algorithms on the prediction process. Mohamed et al. [27] optimized the predicted PV power using the Perturb and Observe and Incremental Conductance algorithms. The optimized PV power can provide energy during transitions of solar radiation. Georgios et al. [28] proposed a model based on criteria that are presented according to the demand to achieve an optimal energy allocation for the predicted PV power generation. To better adapt to widespread application scenarios, online models can be developed based on offline models. The fundamental concept behind methods of online prediction is the necessity

to retrain the prediction model with each prediction iteration, ensuring that the model's network is updated to produce predictions that closely align with actual values.

Table 1. Performance of machine learning methods mentioned in the literature [24].

	Performance Metrics				
Models	**MAPE(%)**	**RMSE(%)**	**nRMSE(%)**	**nMBE(%)**	**SS(%)**
BNN [24]	3.17	53.22	4.53	2.89	78.33
SVR [24]	5.83	81.89	6.37	4.26	63.14
RT [24]	6.27	86.59	7.37	5.42	53.71

A method of online prediction for PV power that is based on PSR, improved GWO, and LSTM is proposed in this paper. Firstly, non-stationary and stationary data are included in PV power data [19,29]. Furthermore, The PV power data are categorized into four seasons according to seasonal characteristics, with eight types of data. SSA is employed to eliminate noise and detect anomalies within PV power sequences. The data processed by SSA is divided into training, validation, and testing datasets. Secondly, the training dataset is utilized to determine the number K of intrinsic mode functions (IMFs) resulting from the CEEMDAN decomposition. The key parameters for the PSR, and the important parameters for LSTM, are determined using the improved GWO, combined with the validation dataset. Thirdly, the online prediction method for PV power acquires parameters that are optimized. The online PV power prediction is also realized. The key contributions of this research are as follows.

1. A novel dynamic adjustment of inertia weight (DAIW) mechanism within the GWO framework is introduced. This enhancement improves the local search capabilities and overall precision of the GWO algorithm, enabling more effective parameter optimization for phase space reconstruction (PSR) and LSTM.
2. An online prediction model that continuously updates and reconstructs the training data using CEEMDAN and PSR at each prediction point is proposed. This real-time adaptation ensures that the LSTM network is consistently trained on the most recent data, enhancing the model's ability to handle dynamic changes in PV power generation.
3. The proposed method is rigorously evaluated against seven alternative prediction models, demonstrating superior performance in terms of accuracy and computational efficiency. This comparative analysis highlights the effectiveness of our integrated approach in achieving higher prediction accuracies.

Section 2 elucidates the theoretical approach utilized in the proposed model. Section 3 outlines the configurations of the strategy for online prediction. Section 4 represents the experimental results realized by the online prediction method and the corresponding analysis. Section 5 outlines the conclusions.

2. Relevant Theories within the Mentioned Methodologies

2.1. Complete Ensemble Empirical Mode Decomposition with Adaptive Noise (CEEMDAN)

The complete ensemble empirical mode decomposition with adaptive noise (CEEMDAN) [17] method was proposed by Torres et al. The PV power data undergoes decomposition via CEEMDAN, producing several datasets, each representing different time scales, known as IMFs. Thus, the prediction accuracy of the subsequent model is improved and the prediction error is decreased. CEEMDAN divides the signal $f(t)$ into several components u_k (where k = 1, 2, 3, …, K), each component u_k possessing a distinct frequency ω_k. The procedural steps of CEEMDAN are outlined below.

Step 1: The PV power sequence is decomposed into K mean-zero white noise, as shown in Equation (1).

$$\boldsymbol{x_i(t) = x(t) + \varepsilon \delta_i(t)} \quad (1)$$

where ε denotes the coefficient of Gaussian white noise weights. $\delta_i(t)$ is the i-th generated white noise.

Step 2: The x_i(t) described above is subjected to an empirical modal decomposition. The first modal component obtained from decomposition is treated as the first modal component obtained from CEEMDAN decomposition. The specific equations are shown in Equations (2) and (3).

$$\boldsymbol{IMF_1}(\boldsymbol{t}) = \frac{\mathbf{1}}{\boldsymbol{K}} \sum_{\boldsymbol{i=1}}^{\boldsymbol{K}} \boldsymbol{IMF_1^i}(\boldsymbol{t}) \tag{2}$$

$$\boldsymbol{r_j}(\boldsymbol{t}) = \boldsymbol{r_{j-1}}(\boldsymbol{t}) - \boldsymbol{IMF_j}(\boldsymbol{t}) \tag{3}$$

where $IMF_1(t)$ represents the first modal component obtained from decomposition. $r_j(t)$ is the signal residual.

Step 3: The specific noise is added to the j-th stage residual obtained from the decomposition, as shown in Equation (4).

$$\boldsymbol{IMF_j}(\boldsymbol{t}) = \frac{\mathbf{1}}{\boldsymbol{K}} \sum_{\boldsymbol{i=1}}^{\boldsymbol{K}} \boldsymbol{E_1}\left\{\boldsymbol{r_{j-1}}(\boldsymbol{t}) + \boldsymbol{\varepsilon_{j-1}}\boldsymbol{E_{j-1}}[\boldsymbol{\delta_i}(\boldsymbol{t})]\right\} \tag{4}$$

where $IMF_j(t)$ is the j-th modal component obtained from decomposition.

Step 4: If the residual signal obtained from the K-th decomposition is monotonous, the procedure of decomposing the signal using CEEMDAN is completed.

2.2. Phase Space Reconstruction (PSR)

PSR is the basis of time series prediction, which is utilized to mine the chaos in time series data. The potential laws governing chaotic time series are investigated through the reconstruction of time series exhibiting chaotic properties into a simplified nonlinear dynamical system [30]. A PSR using a different delay is employed to construct a proper input data sample for the prediction model. The essence of the method is to reconstruct a one-dimensional time series into an m-dimensional phase space vector with time delay τ. The initial one-dimensional PV power history data $P = \{p_i \mid i = 1,2, \ldots, N\}$ can be reconstructed into the m-dimensional phase space using the delayed coordinate method. The forms of m-dimensional phase space are illustrated below.

$$\mathbf{X} = \begin{bmatrix} \mathbf{X_1} & \mathbf{X_2} & \cdots & \mathbf{X_M} \end{bmatrix}^{\mathbf{T}} = \begin{bmatrix} \mathbf{x_1} & \mathbf{x_{1+\tau}} & \cdots & \mathbf{x_{1+(m-1)\tau}} \\ \vdots & \vdots & \ddots & \vdots \\ \mathbf{x_i} & \mathbf{x_{i+\tau}} & \cdots & \mathbf{x_{i+(m-1)\tau}} \\ \vdots & \vdots & \ddots & \vdots \\ \mathbf{x_M} & \mathbf{x_{M+\tau}} & \cdots & \mathbf{x_{M+(m-1)\tau}} \end{bmatrix} \tag{5}$$

where the equation for M can be expressed as $M = N - \tau(m - 1)$. The parameter m is the embedding dimension. The parameter τ denotes time delay. N indicates the number of sample points for the PV power series. X_i denotes the i-th row space vector of the reconstructed phase space species. Moreover, the i-th output point Y_i corresponding to the vector X_i can be expressed as follows:

$$\mathbf{Y} = \begin{bmatrix} \mathbf{Y_1} & \mathbf{Y_2} \cdots & \mathbf{Y_M} \end{bmatrix}^{\mathbf{T}} = \begin{bmatrix} \mathbf{x_{2+(m-1)\tau}} & \mathbf{x_{3+(m-1)\tau}} & \cdots & \mathbf{x_{N+1}} \end{bmatrix}^{\mathbf{T}} \tag{6}$$

In particular, the embedding dimension m and the time delay τ are the key parameters of the PSR. The conventional idea is to determine these two parameters by C-C method [14]. However, the parameters derived from the C-C method have been found to be inconsistent with the actual prediction scenarios during the experimental process. The embedding dimension m and the time delay τ are usually large and with a poor prediction accuracy. Therefore, the improved GWO is utilized to find the optimal PSR m and τ. The specific methods for solving the parameters are described in later sections.

2.3. Grey Wolf Optimization (GWO)

In this paper, GWO [21] is applied in the offline prediction model, which finds the optimal m and τ for PSR. GWO is an intelligent optimization algorithm that is inspired by the leadership hierarchy and hunting mechanism of grey wolves in nature. The grey wolves are categorized into alpha (α), beta (β), delta (δ), and omega (ω) in descending order of rank. The hunting behaviors include searching for prey, encircling prey, hunting, and attacking prey. The most crucial behavior in the predation process of GWO is hunting. The equations for hunting are presented as follows.

$$\begin{cases} \boldsymbol{A_\alpha} = |\boldsymbol{C_1}\cdot\boldsymbol{X_\alpha}(\boldsymbol{t}) - \boldsymbol{X}(\boldsymbol{t})| \\ \boldsymbol{A_\beta} = |\boldsymbol{C_1}\cdot\boldsymbol{X_\beta}(\boldsymbol{t}) - \boldsymbol{X}(\boldsymbol{t})| \\ \boldsymbol{A_\delta} = |\boldsymbol{C_1}\cdot\boldsymbol{X_\delta}(\boldsymbol{t}) - \boldsymbol{X}(\boldsymbol{t})| \end{cases} \tag{7}$$

$$\begin{cases} \boldsymbol{X_1}(\boldsymbol{t}+\boldsymbol{1}) = \boldsymbol{X_\alpha}(\boldsymbol{t}) - \boldsymbol{B_1}\boldsymbol{A_\alpha} \\ \boldsymbol{X_2}(\boldsymbol{t}+\boldsymbol{1}) = \boldsymbol{X_\beta}(\boldsymbol{t}) - \boldsymbol{B_2}\boldsymbol{A_\beta} \\ \boldsymbol{X_3}(\boldsymbol{t}+\boldsymbol{1}) = \boldsymbol{X_\delta}(\boldsymbol{t}) - \boldsymbol{B_2}\boldsymbol{A_\delta} \\ \boldsymbol{X}(\boldsymbol{t}+\boldsymbol{1}) = \frac{\boldsymbol{X_1}(\boldsymbol{t}+\boldsymbol{1})+\boldsymbol{X_2}(\boldsymbol{t}+\boldsymbol{1})+\boldsymbol{X_3}(\boldsymbol{t}+\boldsymbol{1})}{\boldsymbol{3}} \end{cases} \tag{8}$$

where B_1, B_2, and B_3 are the coefficient vectors of α, β and δ, respectively. t is the current iteration number. $X_\alpha(t)$, $X_\beta(t)$, and $X_\delta(t)$ indicate the respective distances between three types of wolves and their prey. $X_1(t+1)$, $X_2(t+1)$, and $X_3(t+1)$ represent the spatial locations of α, β, and δ wolf after t + 1 iterations, respectively. $X(t+1)$ is the spatial location of the ω wolf.

2.4. Long Short-Term Memory Neural Network (LSTM)

LSTM is another RNN neural network, one that was proposed by Hochreiter and Schmidhuber [20]. LSTM can overcome the gradient disappearance problem in RNN neural networks and has more advantages in dealing with long-term dependence. The construction of an LSTM includes a forget gate, input gate, output gate, and cell state. The cell state cooperates with the three gating units to maintain, update and transfer the state information. The calculation equations of LSTM are as follows:

$$\begin{cases} \boldsymbol{f_t} = \mathbf{Sigmoid}(\boldsymbol{\omega_f} \times [\boldsymbol{h_{t-1}}, \boldsymbol{I_t}] + \boldsymbol{\beta_f}) \\ \boldsymbol{i_t} = \mathbf{Sigmoid}(\boldsymbol{\omega_i} \times [\boldsymbol{h_{t-1}}, \boldsymbol{I_t}] + \boldsymbol{\beta_i}) \\ \overline{\boldsymbol{H_t}} = \mathbf{tanh}(\boldsymbol{\omega_c} \times [\boldsymbol{h_{t-1}}, \boldsymbol{I_t}] + \boldsymbol{\beta_c}) \\ \boldsymbol{H_t} = \boldsymbol{f_t} \times \boldsymbol{H_{t-1}} + \boldsymbol{i_t} \times \overline{\boldsymbol{H_t}} \\ \boldsymbol{y_t} = \mathbf{Sigmoid}(\boldsymbol{\omega_o} \times [\boldsymbol{h_{t-1}}, \boldsymbol{I_t}] + \boldsymbol{\beta_o}) \\ \boldsymbol{h_t} = \boldsymbol{y_t}\mathbf{tanh}(\boldsymbol{H_t}) \end{cases} \tag{9}$$

where, f_t is the output of the forget gate at time t; the sigmoid and tanh functions are activation functions; h_{t-1} is the data output information at time $t-1$; I_t is the data input information at time t; ω_f, ω_i, ω_c, and ω_o are weight coefficients; β_f, β_i, β_c, and β_o are bias parameters; i_t and H_t represent input at time t; H_{t-1} is the cell state at time $t-1$; H_t is the cell state at time t; h_t is the data output information at time t; and y_t is the output after activation by the activation function Sigmoid at time t.

3. Online Prediction Methods

The three parts contain data pre-processing, parameter extraction, and online prediction. The overall flowchart is shown in Figure 1.

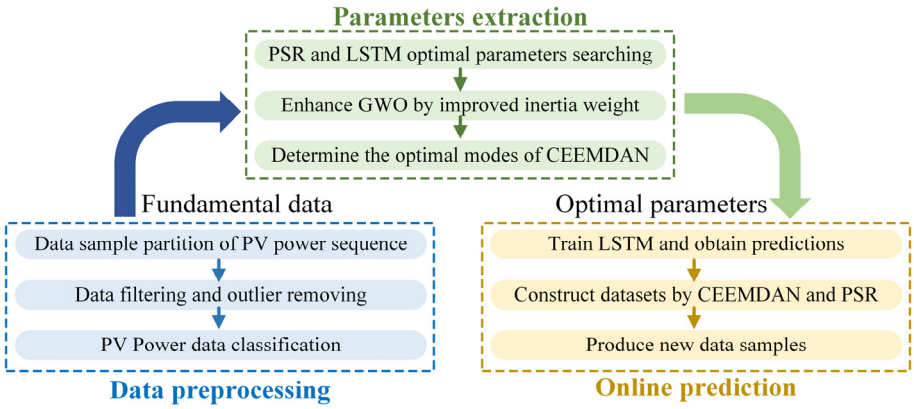

Figure 1. Framework of proposed online prediction method.

3.1. Data Pre-Processing

In the measured PV power data, anomalies exist that are well outside the normal range of fluctuations and which affect the categorization of stationary and non-stationary data. A lot of "burrs" exist in the measured power data, some of which are similar to the noise portion of the signal. Such noise affects the classification of the data and the prediction accuracy of the model. Therefore, the filtering of the PV power data is necessary in the process of data pre-processing.

The PV power data are categorized based on the fluctuation and seasonal characteristics of external ambient. The PV power data, which contains four distinct seasons, can be categorized into stationary and non-stationary types. The daily fluctuation of data can be quantified using the sample entropy (SE) [31], while the average power (P_{mean}) and irradiance (G_{mean}) of each day is computed to serve as a characteristic value representing the fluctuation level of daily power data. SE is a method used to describe the complexity of time series. Compared with P_{mean}, SE more effectively captures the intensity of fluctuations in the input signal. Furthermore, it is not influenced by the size of the dataset and demonstrates good consistency. By computing the daily values of SE, P_{mean} and G_{mean} over a period, a feature matrix is constructed to represent the level of power fluctuations during that time frame. The matrix, where each column of data corresponds to the SE, P_{mean} and G_{mean} values for each day, can be expressed as follows:

$$\begin{bmatrix} \boldsymbol{X}_{ij} \\ \boldsymbol{Y}_{ij} \\ \boldsymbol{Z}_{ij} \end{bmatrix} = \begin{bmatrix} \boldsymbol{x}_{ij}(\mathbf{1}) & \boldsymbol{x}_{ij}(\mathbf{2}) & \boldsymbol{x}_{ij}(\mathbf{3}) & \cdots & \boldsymbol{x}_{ij}(\boldsymbol{d}) \\ \boldsymbol{y}_{ij}(\mathbf{1}) & \boldsymbol{y}_{ij}(\mathbf{2}) & \boldsymbol{y}_{ij}(\mathbf{3}) & \cdots & \boldsymbol{y}_{ij}(\boldsymbol{d}) \\ \boldsymbol{z}_{ij}(\mathbf{1}) & \boldsymbol{z}_{ij}(\mathbf{2}) & \boldsymbol{z}_{ij}(\mathbf{3}) & \cdots & \boldsymbol{z}_{ij}(\boldsymbol{d}) \end{bmatrix} \tag{10}$$

where $\boldsymbol{X}_{ij}$ represent the SE values, $\boldsymbol{Y}_{ij}$ represent the P_{mean} values, and $\boldsymbol{Z}_{ij}$ represents the G_{mean} values. An i of 1 indicates stationary data, and an i of 2 indicates non-stationary data. j denotes the season. j of 1, 2, 3 and 4 denotes the seasons of spring, summer, fall and winter, respectively. d represents the number of days for the current type of data. The reconstruction phase includes grouping and diagonal averaging [32].

To further mitigate noise in PV power data, this research employs singular spectrum analysis (SSA) to filter historical data from PV power sources. SSA is a process for extracting the periodic components of a time series and involves two key phases: decomposition and reconstruction. The decomposition phase includes embedding and singular value decomposition. The filtered data are categorized as datasets of training, verification, and testing. The online prediction of PV power utilizes training and testing datasets. The detailed processes of data pre-processing are illustrated in Figure 2.

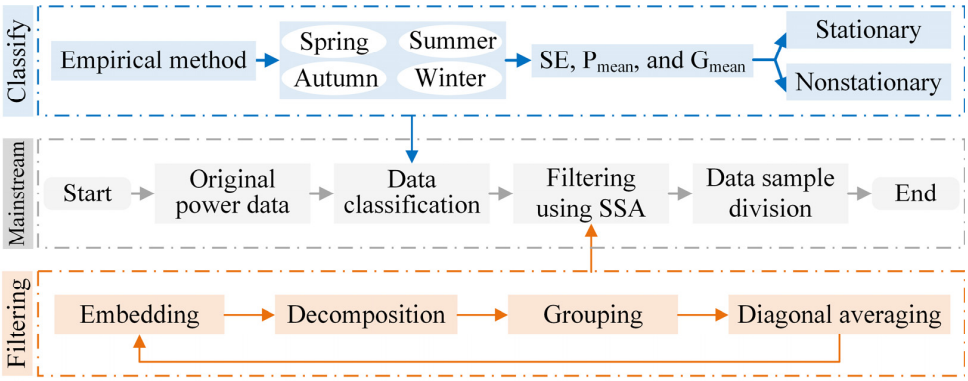

Figure 2. Specific operational processes for data pre-processing.

The theoretical analysis divides annual PV power data into eight categories, reflecting both stationary and non-stationary characteristics for spring, summer, autumn, and winter. Each category is depicted in Figure 3.

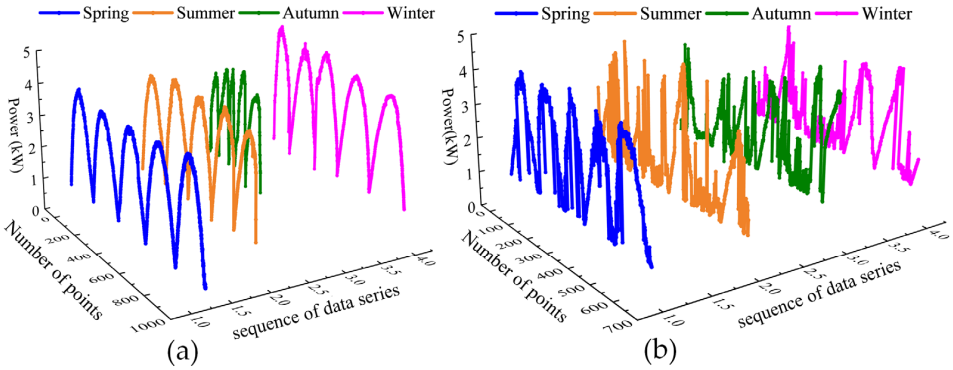

Figure 3. Results of data classification: (**a**) stationary type for PV power data and (**b**) non-stationary type for PV power data.

The SE, P_{mean} and G_{mean} metrics are derived from daily PV measurements. The classification outcomes are presented in Figure 4. The analysis reveals that stationary data tends to possess less fluctuation and greater overall power production. In contrast, non-stationary conditions, with varying ambient irradiance, lead to more significant variations in PV power. The classification method for PV power data introduced has been demonstrated to be effective, offering appropriate reference datasets for predicting PV power.

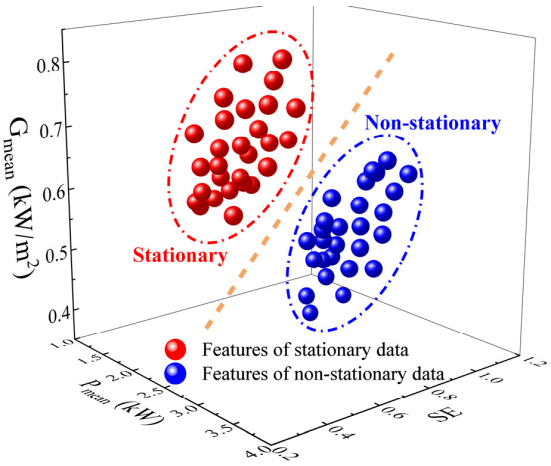

Figure 4. Results of PV power data classification based on SE, P_{mean} and G_{mean}: stationary and non-stationary data.

3.2. Parameter Extraction

The improved GWO is utilized to determine these key parameters for both PSR and LSTM. The classic GWO faces limitations such as inadequate local search capabilities and reduced precision in searching [33]. These shortcomings are addressed in the improved GWO, through the dynamic adjustment of the inertia weight (DAIW) [34].

The m and τ of PSR is determined by the improved GWO. Meanwhile, the important parameters of LSTM are also determined by the improved GWO. The evaluation metric for the fitness function is the root mean square error (RMSE), which measures the discrepancy between predicted and measured PV power. Figure 5 depicts the detailed process of optimizing parameters.

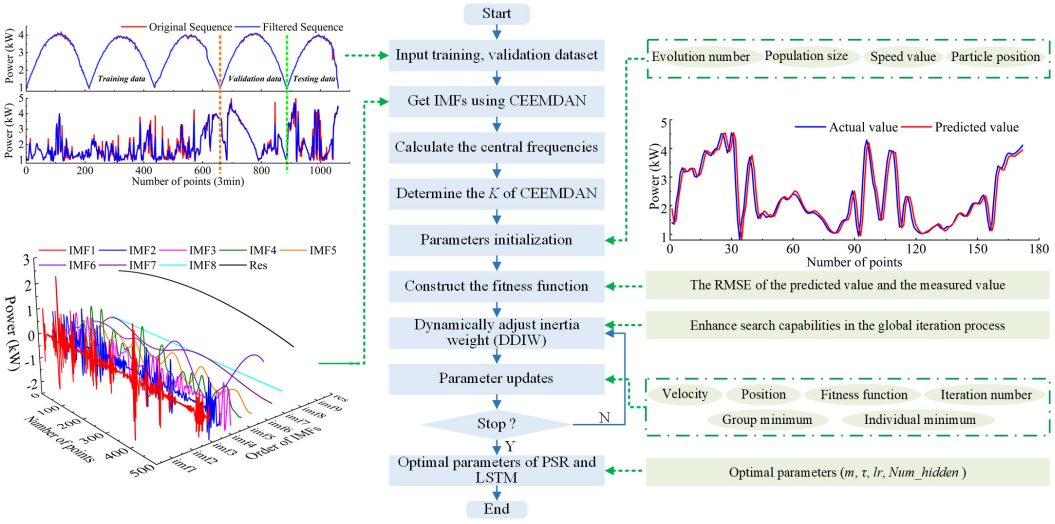

Figure 5. Procedure of parameter extraction for CEEMDAN, PSR, and LSTM.

The DAIW is employed to improve the capability of global searching and decrease the possibilities of the population solution from falling into local optimality, as shown in Equation (11).

$$\boldsymbol{\omega} = \boldsymbol{\omega_{min}} + (\boldsymbol{\omega_{max}} - \boldsymbol{\omega_{min}}) * \boldsymbol{e}^{-\frac{t}{t_{max}}} + \boldsymbol{\sigma} * \boldsymbol{betarnd}(\boldsymbol{p}, \boldsymbol{q}) \quad (11)$$

where the first two items change through an exponential function with a large inertial weight in the early stage, decreasing nonlinearly as the number of iterations increases. The final item adjusts the total value distribution of u using the beta distribution. $\omega_{\min}$ and $\omega_{\max}$ are the respective minimum and maximum inertia weights, with their own respective values of 0.4 and 0.9. t is the current iteration number. $t_{\max}$ represents the maximum number of iterations. Σ represents the inertia adjustment factor, with a value of 0.1, used to control the deviation of the inertia weight. Betarnd (p,q) generates random numbers following a beta distribution. p and q are parameters of the beta distribution, determining the shape of the distribution, and have respective values of 1 and 3.

Initially, the first two components evolve via an exponential function, characterized by a high initial inertial weight that diminishes non-linearly with increasing iterations. The last component employs the beta distribution to modify the distribution of ω. The adjustment factor σ regulates the variance in inertial weight. The DAIW approach refines the adjustment of ω more effectively than other advanced methods such as standard GWO (SGWO), compression factor GWO (CFGWO) [35], and adaptive inertia weighted GWO (AIWGWO) [36]. The equations governing these four inertia weight mechanisms are depicted in Table 2. c_1 and c_2 represent the coefficients used in the CFGWO method. These coefficients determine the influence of individual components in the optimization process. ω_{start} and ω_{end} show the initial and final inertia weight in AIWGWO, respectively. k is the parameter used in the AIWGWO method, influencing the rate of change of the inertia

weight. σ represents the inertia adjustment factor in DAIWGWO, which is used to control the deviation of the inertia weight.

Table 2. Various improved GWOs with their optimal parameter in the process of parameter extraction.

GWO Type	Calculation Equations	Model Parameter	Values
SGWO	$\omega = \omega_{max} - \frac{(\omega_{max}-\omega_{min})\cdot t}{T_{max}}$	ω_{max}, ω_{min}	0.9, 0.4
CFGWO	$\omega = \frac{2}{\left\|2-\varphi-\sqrt{\varphi^2-4\varphi}\right\|}, (\varphi = c_1 + c_2)$	c_1, c_2	1.49, 1.49
AIWGWO	$\omega = (\omega_{start} - \omega_{end})\tan\left(0.875\left(1 - \left(\frac{t}{t_{max}}\right)^k\right)\right)$	$\omega_{start}, \omega_{end}, k$	0.9, 0.4, 0.6
DAIWGWO	$\omega = \omega_{min} + (\omega_{max} - \omega_{min}) * e^{-\frac{t}{t_{max}}} + \sigma * betarnd(p,q)$	$\sigma, \omega_{max}, \omega_{min}, p, q$	0.1, 0.9, 0.4, 1, 3

The objective function utilized for assessing the optimization search performance is presented below:

$$\begin{cases} \boldsymbol{F7}: \boldsymbol{y} = \sum_{i=1}^{n} \boldsymbol{ix_i^4} + \boldsymbol{random}[\boldsymbol{0},\boldsymbol{1}] \\ \boldsymbol{F8}: \boldsymbol{y} = \sum_{i=1}^{n}\left(-\boldsymbol{x_i sin}\left(\sqrt{|\boldsymbol{x_i}|}\right)\right) \\ \boldsymbol{F10}: \boldsymbol{y} = -\boldsymbol{20exp}\left(-\boldsymbol{0.2}\sqrt{\sum_{i=1}^{n}\boldsymbol{x_i^2}}\right) - \boldsymbol{\exp}\left(\frac{\boldsymbol{1}}{\boldsymbol{n}}\sum_{i=1}^{n}\boldsymbol{\cos}(\boldsymbol{2\pi x_i})\right) + \boldsymbol{20} + \boldsymbol{e} \end{cases} \quad (12)$$

For F7, x and y are all in the range of $[-1.28, 1.28]$. For F8, x and y are all in the range of $[-500, 500]$. For F10, x and y are all in the range of $[-32, 32]$. Multiple local extrema exist in Equation (12). The local minimum of Equation (12) is solved using all improved GWOs. Meanwhile, the iteration speed and searching ability for all improved GWOs are compared. Figure 6 displays the iterative procedure for different variations of improved GWO. In Figure 6a, the 3D plot illustrates the landscape of the objective function F7, which is known for its complex and multimodal nature. The corresponding convergence curve in Figure 6b shows the fitness values versus the number of iterations for each GWO variant. It is evident that DAIWGWO (red curve) converges more rapidly to a lower fitness value compared with SGWO, CFGWO, and AIWGWO. This indicates that DAIWGWO is more effective in navigating the complex search space of F7, achieving better optimization performance.

Figure 6c illustrates the 3D landscape of the F8 function, characterized by many local minima. Figure 6d shows the convergence curves for F8, where DAIWGWO again outperforms the other variants, demonstrating efficient search space exploitation. Similarly, Figure 6e depicts the 3D plot of the F10 function's steep landscape. Figure 6f displays the convergence curves for F10, with DAIWGWO showing rapid and stable convergence.

In Figure 6a,c,e, we observe the objective function values (F7, F8 and F10, respectively) plotted against the number of iterations. The iterative curves demonstrate that DAIWGWO converges to a lower objective function value more quickly and consistently compared with the other variants. This indicates superior optimization performance and faster convergence rates. Specifically, Figure 6b,d,f show the iteration process for F7, F8 and F10, respectively, highlighting the stability and efficiency of DAIWGWO in reaching optimal solutions.

Table 3 presents the optimization results for different improved GWO algorithms, comparing their performance in terms of iteration numbers, computation time, and the optimal value achieved for the objective functions F7, F8 and F10. The table reveals that DAIWGWO achieves the optimal value for both F7, F8 and F10, with the fewest iterations and the shortest computation time. Specifically, for the objective function F7, DAIWGWO required only 402 iterations and 2.1473 s to reach an optimal value of 2.52988×10^{-6}, significantly outperforming the other algorithms. Similarly, for F10, DAIWGWO converged in just 60 iterations and 0.5398 s, achieving an optimal value of 4.44089×10^{-16}.

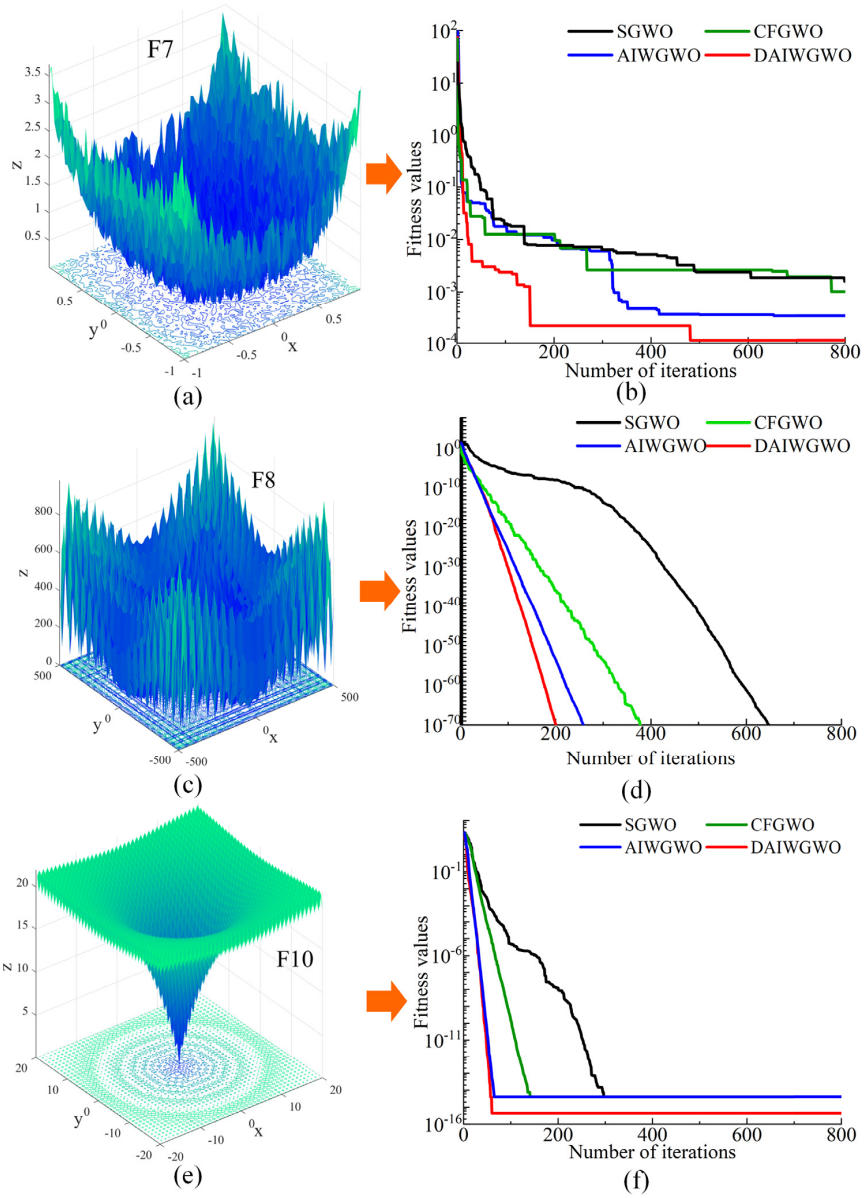

Figure 6. Curves of iterative optimization searching for different optimized PSOs: (**a**) F7, (**b**) iteration process for F7, (**c**) F8, (**d**) iteration process for F8, (**e**) F10, and (**f**) iteration process for F10.

These results demonstrate the efficiency and effectiveness of DAIWGWO in solving complex optimization problems, highlighting its superior performance in terms of both speed and accuracy. The comparative metrics in Table 3 provide a clear indication of the advantages offered by the dynamic adjustment of inertia weights in enhancing the optimization capabilities of the GWO algorithm.

Figure 6 and Table 3 provide critical insights into the performance of different improved GWO algorithms. Figure 6 compares the iterative optimization processes, demonstrating that DAIWGWO achieves faster convergence to optimal solutions compared with SGWO, CFGWO, and AIWGWO. The enhanced convergence rates and stability of DAIWGWO are evident from the iterative curves for each of the objective functions F7, F8 and F10. Overall, the discussions of Figure 6 and Table 3 highlight the significant advancements made by DAIWGWO in optimizing complex functions, thereby justifying its application in our proposed PV power prediction model.

Table 3. Optimization results of different improved *GWO* algorithms.

Models	GWOs	Iteration Numbers	Computation Time (s)	Optimal Value for Objective Function
F7	SGWO	772	2.9856	0.00101
	CFGWO	653	2.3234	0.00186
	AIWGWO	606	2.6732	3.39095×10^{-4}
	DAIWGWO	402	2.1473	2.52988×10^{-6}
F8	SGWO	623	1.3843	8.98604×10^{-70}
	CFGWO	387	1.2154	8.80654×10^{-70}
	AIWGWO	236	0.9845	8.49152×10^{-70}
	DAIWGWO	201	0.8341	8.43281×10^{-70}
F10	SGWO	297	0.8724	9.64051×10^{-10}
	CFGWO	149	0.6237	3.9968×10^{-15}
	AIWGWO	78	0.6998	7.54952×10^{-15}
	DAIWGWO	60	0.5398	4.44089×10^{-16}

3.3. Online Prediction Method

Firstly, the training dataset undergoes decomposition via CEEMDAN, selecting the parameter K during the offline parameter extraction phase. Based on the content of Section 2.1 and in combination with the training data, we set K to 11. LSTM is then trained using these reconstructed datasets and subsequently utilized to predict the values for each IMF.

For the second prediction cycle, the training dataset is updated by incorporating the previously predicted value and removing the oldest measured point to keep the dataset size constant, ensuring the stability of the decomposition results. The updated training set is re-decomposed using CEEMDAN, followed by new predictions through PSR and LSTM. This process repeats iteratively until all data points in the testing dataset are predicted. The ultimate online prediction outcomes are acquired by amalgamating the predicted values across all IMFs, illustrated in Figure 7. The above procedure of online prediction systematically improves prediction accuracy and adapts to new data inputs.

3.4. Evaluation Metrics for Prediction Models

The paper employs four evaluation metrics to comprehensively assess the performance differences among the PV power prediction algorithms used. The four evaluation metrics utilized are RMSE, mean absolute percentage error (MAPE), coefficient of determination (R^2), and calculation time (C_{time}). The specific equations are shown as follows:

$$\boldsymbol{RMSE} = \sqrt{\frac{1}{N}\sum_{i=1}^{N}\left(T_i - T_i'\right)^2} \tag{13}$$

$$\boldsymbol{MAPE} = \frac{1}{N}\sum_{i=1}^{N}\left|\frac{\left(T_i - T_i'\right)}{Y_i}\right| \times 100\% \tag{14}$$

$$\boldsymbol{R^2} = 1 - \frac{\sum\left(T_i - T_i'\right)^2}{\sum\left(T_i - \overline{T}\right)^2} \tag{15}$$

where T_i and T_i' are the measured and prediction data for PV power, respectively. N presents the number of power points for the testing dataset.

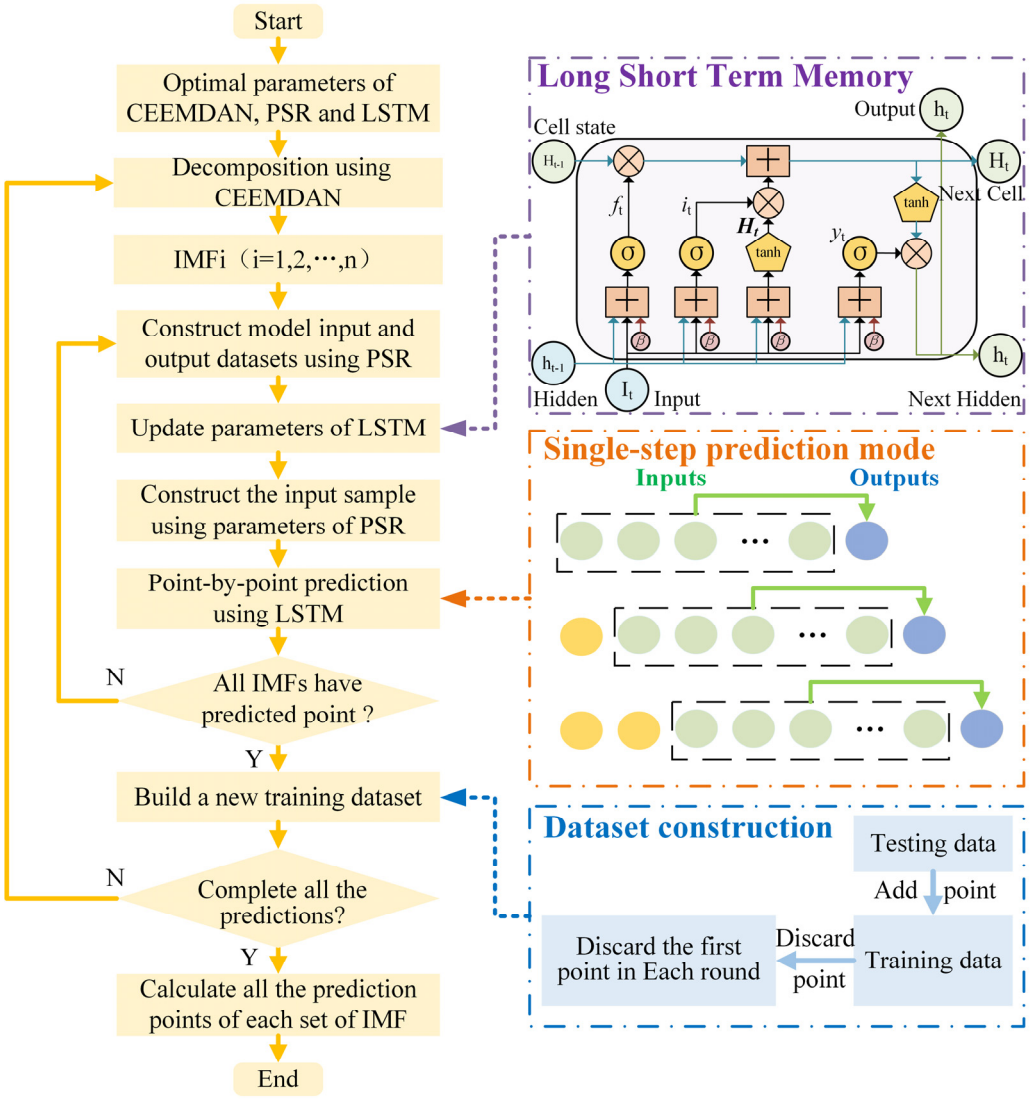

Figure 7. Procedure for the online prediction of PV power.

4. Experimental Results and Analysis

The PV power data are obtained from a PV power station with a generating capacity of 10 kW. The specific experimental site is located in Nanjing, China. Nanjing's geographical coordinates are 31°14′–32°37′ N, 118°22′–119°14′ E, situated in a subtropical monsoon climate. The measurement equipment for I–V characteristics includes the tested PV array, an I–V data measurement module, temperature sensors, a pyranometer, computers, and monitoring software. The PV array used consists of 32 PV modules. The collected PV power data span three years, from 2018 to 2020.

4.1. Description of the Experimental Data for Pre-Processing

Theoretical analysis categorizes annual PV power data into eight distinct types, including both stationary and non-stationary sets across spring, summer, autumn, and winter, as shown in Figure 3. Daily PV power calculations yield SE, P_{mean} and G_{mean} values, with classification outcomes depicted in Figure 4.

For both stationary and non-stationary data, five-day segments are selected as the basis for subsequent experiments, with each dataset comprising 1062 data points. SSA is employed to remove noise and outliers from these sequences. These five-day periods for both data types are systematically divided into datasets of training, validation, and testing.

4.2. Experimental Results of Parameter Extraction

Utilizing the improved GWO aids in identifying the optimal parameters for PSR and LSTM, laying the theoretical groundwork for feature selection in online prediction methodologies. The outcomes of the parameter optimization are summarized in Table 4.

Table 4. Optimal parameters of stationary and non-stationary data for PV power.

Stationary Data for PV Power				Non-Stationary Data for PV Power			
m	τ	*lr*	*Num_hidden*	*m*	τ	*lr*	*Num_hidden*
2	4	196.67	19.33	1	5	781.58	602.34

4.3. Online Prediction Model Calculation Results

4.3.1. Comparative Evaluation of Various Fundamental Prediction Models

All evaluation metrics and power prediction algorithms are implemented on the MATLAB 2023b platform. The corresponding computational environment is configured with an Intel I7-8570 processor, running at 2.2 GHz, with 16.0 GB of RAM, and using the Windows 10 operating system.

The fundamental prediction model plays a crucial role in the online PV power prediction methodology. Meanwhile, the utilization of a kernel function ensures the stability of the model mapping outcomes. LSTM is selected as the essential component of online PV power prediction in this paper. The performance of seven prediction models is compared to verify the prediction advantages of LSTM. Seven prediction models contain BP [37], ELM, LSTM, Elman [38], SVM, Volterra [39], and KELM. In order to better reflect the performance of the algorithms, R^2 can be utilized to represent the fitting performance of PV power prediction methods. RMSE and MAPE are employed to reflect the prediction accuracy of PV power prediction methods. Computation time is used to evaluate the computation cost of the algorithms. The RMSE, MAPE, and C_{time} are transformed using an exponential function, whereas R^2 is subjected to a sigmoid function. [19]. After the above normalization, all metric outcomes are scaled within the range of 0 to 1. The specific equations are presented in Equations (16) and (17). The customized evaluation metrics show a direct link to the model's predictive accuracy. Consequently, these metrics are integrated to formulate a unified comprehensive evaluation metric.

The processed evaluation metrics exhibit a positive correlation with the prediction performance of the model. Therefore, the processed evaluation metrics are combined to derive a comprehensive evaluation metric. The comparison results for various methods are presented in Figure 8.

$$\boldsymbol{P}(\boldsymbol{x}) = \frac{\mathbf{1}}{(\mathbf{1} + \boldsymbol{e}^{-\boldsymbol{x}})} \tag{16}$$

$$\boldsymbol{P}(\boldsymbol{y}) = \frac{\mathbf{1}}{\boldsymbol{e}^{\boldsymbol{y}}} \tag{17}$$

where the values of x correspond to the values of R^2. The values of RMSE, MAPE and computational time are set as y. To ensure consistency in computational time across other evaluation metrics, it is suggested to normalize the computational time by dividing it by 100 before incorporating it into Equation (17) for computation. This adjustment ensures that the computational time remains in a similar order of magnitude as the other processed evaluation metrics. The analysis results of prediction performance for various methods are illustrated in Figure 8.

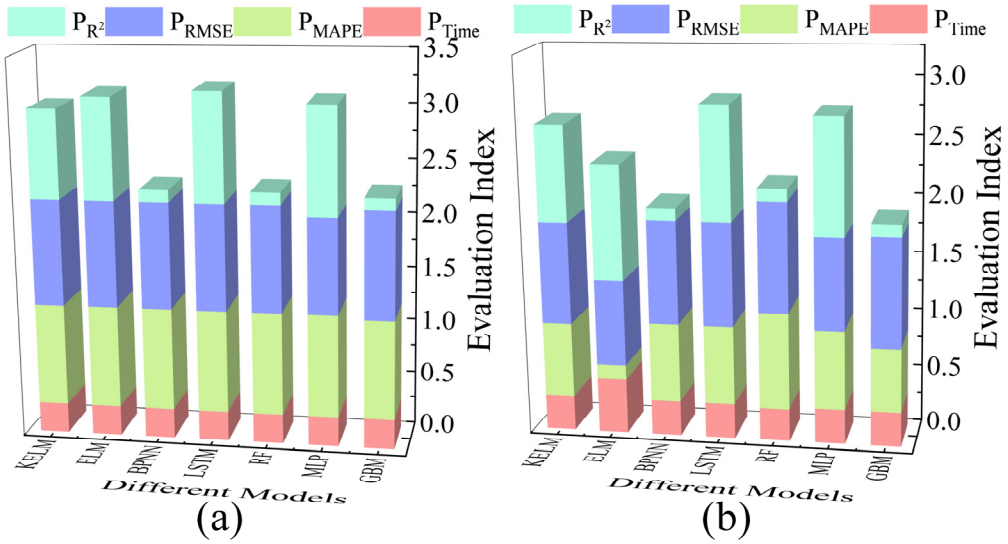

Figure 8. Performance comparison results of basic models: (**a**) evaluation results for stationary data and (**b**) evaluation results for non-stationary data.

P_{time}, P_{RMSE}, P_{MAPE}, P_{R2} are assessment metrics corresponding to the predictive outcomes of different methodologies. As the performance of the prediction method improves, the values of these metrics increase. The post-processed evaluation metrics are positively correlated with the predictive performance of the models. By combining the post-processed evaluation metrics, a comprehensive evaluation index is obtained. A higher value of the comprehensive evaluation index indicates stronger performance of the corresponding method. P_{time}, P_{RMSE}, P_{MAPE}, P_{R2} are evaluation metrics that correspond to the prediction results of various methods. For stationary data, LSTM achieves the highest comprehensive evaluation index value. Due to the relatively stable weather data and good quality of PV power data, there is not much difference in predictive performance among the various algorithms. Compared with the other algorithms, ELM and Volterra exhibit slightly lower predictive performance than LSTM. Non-stationary data exhibit larger fluctuations and lower quality compared with stationary data. Figure 8b clearly demonstrates that the comprehensive evaluation index value of LSTM is significantly higher than that of the other six algorithms.

4.3.2. Comparison of Predictive Outcomes from Various Methodologies

The decomposing of PV power data is treated by CEEMDAN in the process of online prediction. To validate the effectiveness of the proposed method, denoted as CEEMDAN -DAIWGWO-PSR-LSTM, this paper compares its performance with several existing techniques in predicting PV power. Specifically, SVM, Elman, LSTM, PSR-LSTM, CEEMDAN -LSTM, CEEMDAN-PSR-LSTM, CEEMDAN-GWO-PSR-LSTM, and the proposed method are employed for prediction, followed by a comprehensive comparison of their prediction results. The experiment results aim to verify the superiority of the proposed method. The initial three prediction methods outperformed others in previous analyses and were thus chosen as benchmarks. LSTM stands out due to its rapid and stable computational performance, along with a distinctive calculation principle. Subsequent experimental findings highlight the superiority of LSTM, cementing its status as the foundational model for the online prediction technique outlined in this paper.

Figure 9 depicts the prediction outcomes of various methods in online mode. Tables 5 and 6 present the performance metrics for the stationary and non-stationary data of PV power, respectively. The methods used in the experiment contain SVM, Elman, LSTM, PSR-LSTM, CEEMDAN-PSR- LSTM, and CEEMDAN-GWO-PSR-LSTM. The proposed method exhibits significant advantages in R^2 and in RMSE based on prediction power curves and evaluation metrics. Compared with SVM, the variability in the R^2 for

the stationary type is reduced. However, the RMSE of CEEMDAN-DAIWGWO-PSR-LSTM is 0.0843 kW less than that of SVM.

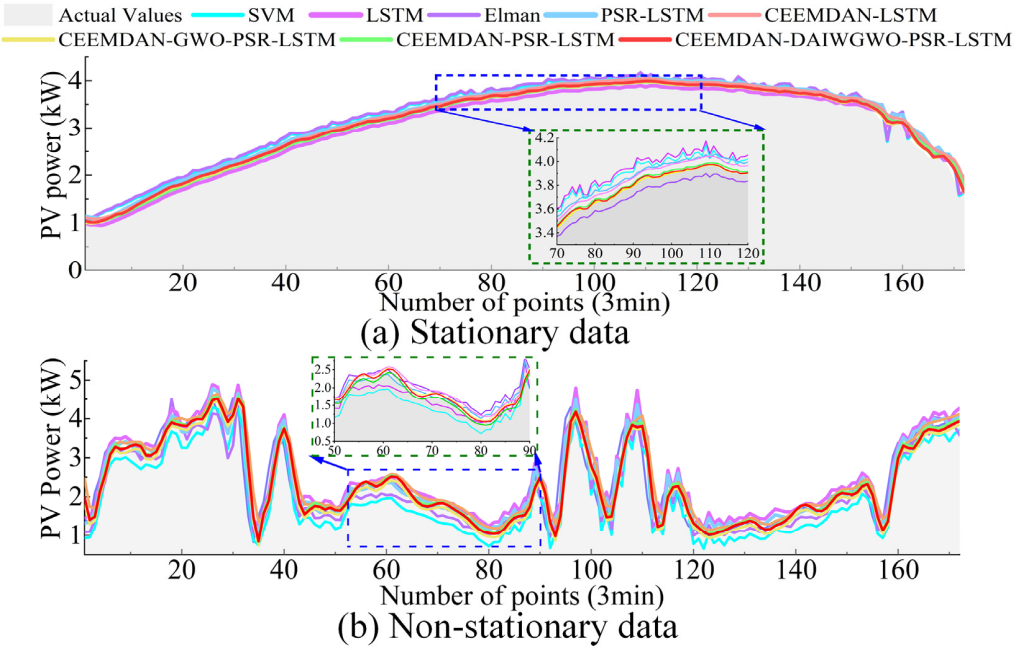

Figure 9. Comparative analysis of prediction results using various methods for PV power sequences in spring: (**a**) stationary data for PV power and (**b**) non-stationary data for PV power.

Table 5. Evaluation results of the prediction of stationary data for PV power in spring.

Models	R^2	RMSE (kW)	Time (s)
SVM [18]	0.9819	0.1261	416.5239
Elman [39]	0.9820	0.1476	382.6941
LSTM [20]	0.9826	0.1255	358.3088
PSR-LSTM	0.9845	0.1147	363.5018
CEEMDAN-LSTM	0.9804	0.1063	400.2096
CEEMDAN-PSR-LSTM	0.9823	0.0767	444.2270
CEEMDAN-GWO-PSR-LSTM	0.9963	0.0529	499.3937
CEEMDAN-DAIWGWO-PSR-LSTM	0.9974	0.0418	402.4795

Table 6. Evaluation results of the prediction of non-stationary data for PV power in spring.

Models	R^2	RMSE (kW)	Time (s)
SVM [18]	0.8082	0.4730	384.4777
Elman [39]	0.7841	0.4028	373.6857
LSTM [20]	0.8458	0.3915	372.2496
PSR-LSTM	0.8666	0.3966	375.4598
CEEMDAN-LSTM	0.8730	0.3768	495.8506
CEEMDAN-PSR-LSTM	0.8664	0.3762	491.3453
CEEMDAN-GWO-PSR-LSTM	0.8714	0.3694	496.8043
CEEMDAN-DAIWGWO-PSR- LSTM	0.8966	0.3621	495.8506

The proposed method demonstrates more stability in R^2 for stationary data relative to SVM. Additionally, it exhibits a reduction in RMSE by 0.0843 kW, compared with that of SVM. Moreover, there are improvements of approximately 67% and 79% in their respective proportions. For the non-stationary type, R^2 increases by 0.0884 and the RMS decreases by 0.1109 kW. The improvement of R^2, and RMSE is about 11%, and 23% compared with SVM, respectively.

Moreover, LSTM exhibits distinct advantages compared with Elman and SVM. The integration of CEEMDAN with LSTM notably enhances the prediction results. In comparison with LSTM, CEEMDAN-LSTM yields reductions of 0.0192 kW in RMSE for stationary PV power data. For the non-stationary data of PV power, the values of R^2 increase by 0.0272 and the RMSE decreases by 0.0147 kW. The integration of PSR, and DAIWGWO enhances the accuracy of the online prediction method across various levels.

The method proposed in this paper achieves an average computation time of 469 s, predicting 172 data points at roughly 3 s per point. The data are sampled at intervals of 3 min. Accordingly, CEEMDAN-DAIWGWO-PSR-LSTM is well-adapted for the online prediction of PV power. Moreover, the extra time consumed during the prediction phase by this method, when compared with alternative approaches, does not significantly affect the prediction outcomes and can be considered negligible.

The aforementioned experimental findings depict the prediction results for both stationary and non-stationary state PV power data during the spring season. To provide further insights into the prediction outcomes for the remaining seasons, this study conducted experiments on the prediction scenarios for both stationary and non-stationary PV power data during the summer season. The prediction results for the summer season are illustrated in Figure 10 and summarized in Table 7. Regarding the enlarged section of Figure 10, it is evident that the proposed prediction method, CEEMDAN-DAIWGWO-PSR-LSTM, closely approximates the original data compared with other methods. For stationary data during the summer season, the R^2 and RMSE values for CEEMDAN-DAIWGWO-PSR-LSTM are 0.9907, and 0.0511 kW, respectively. For non-stationary data during the summer season, the R^2 and RMSE values for CEEMDAN-DAIWGWO-PSR-LSTM are 0.9042, and 0.2776 kW, respectively. The evaluation metrics demonstrate that the proposed prediction method outperforms the other algorithms. Table 7 also presents the evaluation metric results for the autumn and winter seasons. The prediction outcomes for the remaining two seasons align with the conclusions drawn from the earlier prediction results for the spring and summer seasons. The online PV power prediction method proposed in this study exhibits significant predictive advantages, establishing itself as an effective and efficient prediction approach.

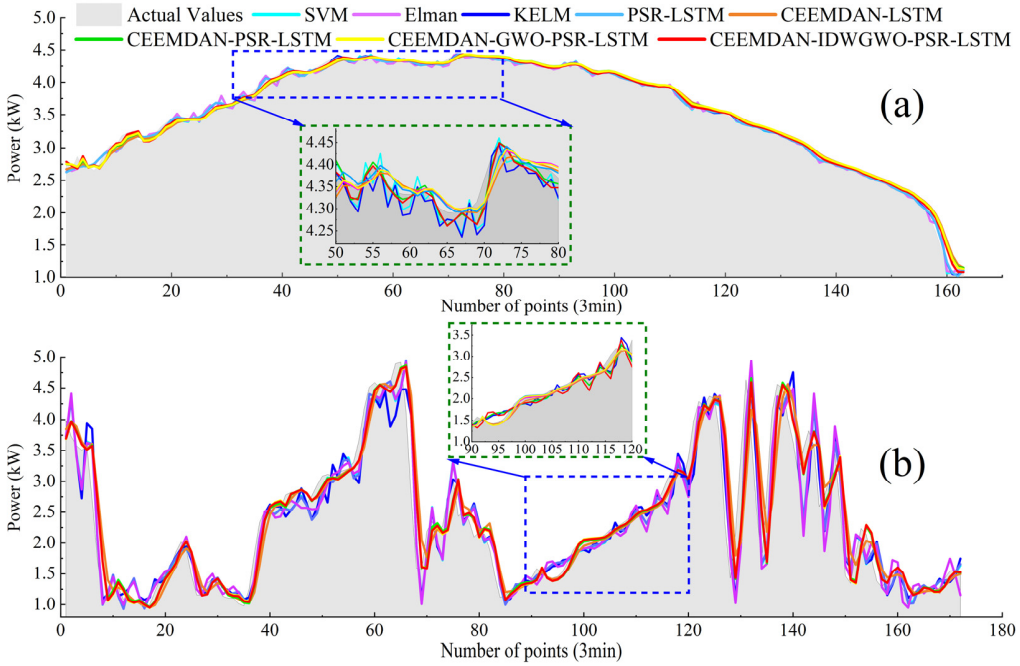

Figure 10. Prediction results of the stationary and non-stationary PV power in summer: (**a**) stationary data for PV power and (**b**) non-stationary data for PV power.

Table 7. Evaluation outcomes for predictive methods across the remaining three seasons.

Types	Models	Stationary Data for PV Power		Non-Stationary Data for PV Power	
		R^2	RMSE (kW)	R^2	RMSE (kW)
Summer	SVM [18]	0.9860	0.1013	0.8142	0.4709
	Elman [39]	0.9853	0.1373	0.8169	0.4399
	LSTM [20]	0.9858	0.1102	0.8646	0.4809
	PSR-LSTM	0.9859	0.1159	0.8745	0.4223
	CEEMDAN-LSTM	0.9842	0.0970	0.8606	0.3992
	CEEMDAN-PSR-LSTM	0.9883	0.0825	0.8639	0.4008
	CEEMDAN-GWO-PSR-LSTM	0.9984	0.0622	0.9093	0.3749
	CEEMDAN-DAIWGWO-PSR-LSTM	0.9907	0.0511	0.9042	0.2776
Autumn	SVM [18]	0.9750	0.1289	0.8916	0.3848
	Elman [39]	0.9750	0.1199	0.8885	0.3710
	LSTM [20]	0.9843	0.1109	0.8919	0.2944
	PSR-LSTM	0.9847	0.1198	0.8895	0.2868
	CEEMDAN-LSTM	0.9880	0.1191	0.9574	0.2101
	CEEMDAN-PSR-LSTM	0.9846	0.0991	0.9663	0.1964
	CEEMDAN-GWO-PSR-LSTM	0.9944	0.0804	0.9679	0.1820
	CEEMDAN-DAIWGWO-PSR-LSTM	0.9954	0.0727	0.9694	0.1776
Winter	SVM [18]	0.9766	0.1383	0.9231	0.3007
	Elman [39]	0.9757	0.1426	0.9220	0.3958
	LSTM [20]	0.9860	0.1393	0.9583	0.2968
	PSR-LSTM	0.9868	0.1280	0.8728	0.4010
	CEEMDAN-LSTM	0.9852	0.1079	0.8816	0.2718
	CEEMDAN-PSR-LSTM	0.9834	0.0971	0.9383	0.2687
	CEEMDAN-GWO-PSR-LSTM	0.9859	0.0937	0.9491	0.2383
	CEEMDAN-DAIWGWO-PSR- LSTM	0.9918	0.0837	0.9513	0.2047

In terms of PV power dynamics, non-stationary power in summer exhibits more significant fluctuations compared with autumn and winter. It is also noted that the R^2 value for summer's non-stationary PV power prediction is lower than those for autumn and winter. Correspondingly, the RMSE values for summer are higher, aligning with the observed trends in the power curves. For stationary PV power forecasts, the curves produced by our method are closely matched with actual measured data. When dealing with non-stationary PV power, predictions inevitably face delays, primarily due to substantial fluctuations in power levels. However, the proposed method, which integrates CEEMDAN and PSR, significantly reduces these delays. This improvement is attributed to the effective mitigation or elimination of chaotic characteristics in the PV power data through CEEMDAN and PSR. Regardless of whether the PV power type is stationary or non-stationary, the prediction power curves produced by CEEMDAN-DAIWGWO-PSR-LSTM exhibit high fidelity to the measured curves, while minimizing prediction delays.

5. Conclusions

In this study, we proposed a novel real-time prediction method for photovoltaic (PV) power using an improved grey wolf optimization (GWO) algorithm combined with a long short-term memory (LSTM) neural network. The key contributions and findings of our research are as follows.

1. We introduced the dynamic adjustment of inertia weight GWO (DAIWGWO) algorithm, which enhances the balance between exploration and exploitation. The dynamic adjustment mechanism significantly improves convergence speed and optimization accuracy.
2. The integration of DAIWGWO with an LSTM neural network effectively captures the temporal dependencies and non-linear characteristics of PV power data. This combination leads to highly accurate real-time predictions.

3. Our method was rigorously evaluated using multiple benchmark functions and real-world PV power data. The results demonstrate that DAIWGWO outperforms traditional GWO variants and other benchmark methods in terms of prediction accuracy and computational efficiency.
4. The proposed method's ability to provide accurate real-time predictions of PV power makes it highly suitable for practical applications in energy management and grid stability.

Overall, the DAIWGWO-LSTM model presents a robust and efficient solution for real-time PV power prediction, offering significant advancements over existing approaches. Future work will focus on further optimizing the model and exploring its applicability to other renewable energy sources.

Author Contributions: Methodology, X.L.; Software, Y.G.; Validation, J.L.; Formal analysis, W.Y.; Resources, J.S.; Data curation, J.D. All authors have read and agreed to the published version of the manuscript.

Funding: This research was funded by State Grid science and technology project grant number SGLNYXOODFJS2310095.

Data Availability Statement: Data are contained within the article.

Conflicts of Interest: The authors declare no conflict of interest.

Abbreviations

AIWGWO	Adaptive inertia weighted GWO	MAPE	Absolute percentage error
BNN	Bayesian neural networks	NWP	Numerical weather prediction
CEEMDAN	Complete ensemble empirical mode decomposition with adaptive noise	P_{mean}	Average power
CFGWO	Compression factor GWO	PSR	Phase space reconstruction
C_{time}	Calculation time	PV	Photovoltaic
DAIWGWO	Dynamic adjustment of the inertia weight GWO	R^2	Coefficient of determination
EMD	Empirical mode decomposition	RMSE	Root mean square error
EEMD	Ensemble empirical mode decomposition	RT	Regression tree
FCM	Fuzzy C-means	SE	Sample entropy
GA-BP	Genetic algorithm-back propagation	SGWO	Standard GWO
G_{mean}	Average irradiance	SSA	Singular spectrum analysis
GWO	Grey wolf optimization	SVM	Support vector machine
IMFs	Intrinsic mode functions	SVR	Support vector machine regression
KELM	Kernel-based extreme learning machine	WD	Wavelet decomposition
LSSVM	Least squares support vector machine	WOA	Whale optimization algorithm
LSTM	Long short-term memory		

References

1. Liu, Z.-F.; Li, L.-L.; Tseng, M.-L.; Lim, M.K. Prediction Short-Term Photovoltaic Power Using Improved Chicken Swarm Optimizer—Extreme Learning Machine Model. *J. Clean. Prod.* **2020**, *248*, 119272. [CrossRef]
2. Brester, C.; Kallio-Myers, V.; Lindfors, A.V.; Kolehmainen, M.; Niska, H. Evaluating Neural Network Models in Site-Specific Solar PV Forecasting Using Numerical Weather Prediction Data and Weather Observations. *Renew. Energy* **2023**, *207*, 266–274. [CrossRef]
3. Ahn, H. A Framework for Developing Data-Driven Correction Factors for Solar PV Systems. *Energy* **2024**, *290*, 130096. [CrossRef]
4. Mayer, M.J.; Gróf, G. Extensive Comparison of Physical Models for Photovoltaic Power Forecasting. *Appl. Energy* **2021**, *283*, 116239. [CrossRef]
5. Moreira, M.O.; Balestrassi, P.P.; Paiva, A.P.; Ribeiro, P.F.; Bonatto, B.D. Design of Experiments Using Artificial Neural Network Ensemble for Photovoltaic Generation Forecasting. *Renew. Sustain. Energy Rev.* **2021**, *135*, 110450. [CrossRef]

6. Souabi, S.; Chakir, A.; Tabaa, M. Data-Driven Prediction Models of Photovoltaic Energy for Smart Grid Applications. *Energy Rep.* **2023**, *9*, 90–105. [CrossRef]
7. Liao, Z.; Min, W.; Li, C.; Wang, B. Photovoltaic Power Prediction Based on Irradiation Interval Distribution and Transformer-LSTM. *Energies* **2024**, *17*, 2969. [CrossRef]
8. Keddouda, A.; Ihaddadene, R.; Boukhari, A.; Atia, A.; Arıcı, M.; Lebbihiat, N.; Ihaddadene, N. Photovoltaic Module Temperature Prediction Using Various Machine Learning Algorithms: Performance Evaluation. *Appl. Energy* **2024**, *363*, 123064. [CrossRef]
9. Li, P.; Zhou, K.; Lu, X.; Yang, S. A Hybrid Deep Learning Model for Short-Term PV Power Forecasting. *Appl. Energy* **2020**, *259*, 114216. [CrossRef]
10. Hu, Z.; Gao, Y.; Ji, S.; Mae, M.; Imaizumi, T. Improved Multistep Ahead Photovoltaic Power Prediction Model Based on LSTM and Self-Attention with Weather Forecast Data. *Appl. Energy* **2024**, *359*, 122709. [CrossRef]
11. Pan, G.; Ma, D.; Sun, H.; Zhao, Y.; Ouyang, J.; Merveille, M.K.; Wu, X. Modeling Optimization Method Based on Gamma Test and NSGA II for Forecast of PV Power Output. *Int. J. Green Energy* **2022**, *19*, 967–976. [CrossRef]
12. Wang, X.; Ma, W. A Hybrid Deep Learning Model with an Optimal Strategy Based on Improved VMD and Transformer for Short-Term Photovoltaic Power Forecasting. *Energy* **2024**, *295*, 131071. [CrossRef]
13. Zang, H.; Liu, L.; Sun, L.; Cheng, L.; Wei, Z.; Sun, G. Short-Term Global Horizontal Irradiance Forecasting Based on a Hybrid CNN-LSTM Model with Spatiotemporal Correlations. *Renew. Energy* **2020**, *160*, 26–41. [CrossRef]
14. Wang, Y.; Zhu, L.; Xue, H. Ultra-Short-Term Photovoltaic Power Prediction Model Based on the Localized Emotion Reconstruction Emotional Neural Network. *Energies* **2020**, *13*, 2857. [CrossRef]
15. Gao, H.; Qiu, S.; Fang, J.; Ma, N.; Wang, J.; Cheng, K.; Wang, H.; Zhu, Y.; Hu, D.; Liu, H.; et al. Short-Term Prediction of PV Power Based on Combined Modal Decomposition and NARX-LSTM-LightGBM. *Sustainability* **2023**, *15*, 8266. [CrossRef]
16. Wang, L.; Mao, M.; Xie, J.; Liao, Z.; Zhang, H.; Li, H. Accurate Solar PV Power Prediction Interval Method Based on Frequency-Domain Decomposition and LSTM Model. *Energy* **2023**, *262*, 125592. [CrossRef]
17. Li, M.; Wang, W.; He, Y.; Wang, Q. Deep Learning Model for Short-Term Photovoltaic Power Forecasting Based on Variational Mode Decomposition and Similar Day Clustering. *Comput. Electr. Eng.* **2024**, *115*, 109116. [CrossRef]
18. Zhang, C.; Xu, M. Time-Segment Photovoltaic Forecasting and Uncertainty Analysis Based on Multi-Objective Slime Mould Algorithm to Improve Support Vector Machine. *IEEE Trans. Power Syst.* **2024**, *39*, 5103–5114. [CrossRef]
19. Chen, X.; Ding, K.; Zhang, J.; Han, W.; Liu, Y.; Yang, Z.; Weng, S. Online Prediction of Ultra-Short-Term Photovoltaic Power Using Chaotic Characteristic Analysis, Improved PSO and KELM. *Energy* **2022**, *248*, 123574. [CrossRef]
20. Zhen, H.; Niu, D.; Wang, K.; Shi, Y.; Ji, Z.; Xu, X. Photovoltaic Power Forecasting Based on GA Improved Bi-LSTM in Microgrid without Meteorological Information. *Energy* **2021**, *231*, 120908. [CrossRef]
21. Wang, Y.; Yang, Q.; Xue, H.; Mi, Y.; Tu, Y. Ultra-Short-Term PV Power Prediction Model Based on HP-OVMD and Enhanced Emotional Neural Network. *IET Renew. Power Gener.* **2022**, *16*, 2233–2247. [CrossRef]
22. Zhang, J.; Hao, Y.; Fan, R.; Wang, Z. An Ultra-Short-Term PV Power Forecasting Method for Changeable Weather Based on Clustering and Signal Decomposition. *Energies* **2023**, *16*, 3092. [CrossRef]
23. Gu, B.; Shen, H.; Lei, X.; Hu, H.; Liu, X. Forecasting and Uncertainty Analysis of Day-Ahead Photovoltaic Power Using a Novel Forecasting Method. *Appl. Energy* **2021**, *299*, 117291. [CrossRef]
24. Theocharides, S.; Theristis, M.; Makrides, G.; Kynigos, M.; Spanias, C.; Georghiou, G.E. Comparative Analysis of Machine Learning Models for Day-Ahead Photovoltaic Power Production Forecasting. *Energies* **2021**, *14*, 1081. [CrossRef]
25. Ibrahim, I.A.; Hossain, M.J.; Duck, B.C. An Optimized Offline Random Forests-Based Model for Ultra-Short-Term Prediction of PV Characteristics. *IEEE Trans. Ind. Inform.* **2020**, *16*, 202–214. [CrossRef]
26. Ibrahim, C.; Reboul, J.-M.; Houivet, D.; Gualous, H. A Comparison of Power Plant Energy Flow Prediction Using Real Data Applied to Linear Programming and If-Else Algorithms. *Energy Rep.* **2023**, *9*, 294–300. [CrossRef]
27. Louzazni, M.; Cotfas, D.T.; Cotfas, P.A. Management and Performance Control Analysis of Hybrid Photovoltaic Energy Storage System under Variable Solar Irradiation. *Energies* **2020**, *13*, 3043. [CrossRef]
28. Arnaoutakis, G.E.; Kocher-Oberlehner, G.; Katsaprakakis, D.A. Criteria-Based Model of Hybrid Photovoltaic–Wind Energy System with Micro-Compressed Air Energy Storage. *Mathematics* **2023**, *11*, 391. [CrossRef]
29. Jiang, M.; Ding, K.; Chen, X.; Cui, L.; Zhang, J.; Yang, Z.; Cang, Y.; Cao, S. Research on Time-Series Based and Similarity Search Based Methods for PV Power Prediction. *Energy Convers. Manag.* **2024**, *308*, 118391. [CrossRef]
30. Zheng, L.; Su, R.; Sun, X.; Guo, S. Historical PV-Output Characteristic Extraction Based Weather-Type Classification Strategy and Its Forecasting Method for the Day-Ahead Prediction of PV Output. *Energy* **2023**, *271*, 127009. [CrossRef]
31. Li, Z.; Xu, R.; Luo, X.; Cao, X.; Du, S.; Sun, H. Short-Term Photovoltaic Power Prediction Based on Modal Reconstruction and Hybrid Deep Learning Model. *Energy Rep.* **2022**, *8*, 9919–9932. [CrossRef]
32. Sado, T.; Motz, Z.; Yentes, J.M.; Mukherjee, M. Passive Exoskeleton-Assisted Gait Shows a Unique Interlimb Coordination Signature Without Restricting Regular Walking. *Front. Physiol.* **2022**, *13*, 916185. [CrossRef] [PubMed]
33. Du, Y.; Xu, F. A Hybrid Multi-Step Probability Selection Particle Swarm Optimization with Dynamic Chaotic Inertial Weight and Acceleration Coefficients for Numerical Function Optimization. *Symmetry* **2020**, *12*, 922. [CrossRef]
34. Xu, J.; Wang, R.; Zhang, Q.; Cui, T.; Li, H.; Pei, L.; Quan, X. Design of Engine Cooling System Using Improved Particle Swarm Optimization Algorithm. *IEEE Sens. J.* **2023**, *23*, 19060–19072. [CrossRef]

35. Wang, B.; Wang, X.; He, M.; Zhu, X. Study on Multi-Model Soft Sensor Modeling Method and Its Model Optimization for the Fermentation Process of Pichia Pastoris. *Sensors* **2021**, *21*, 7635. [CrossRef]
36. Anbarasi, M.P.; Kanthalakshmi, S. Power Maximization in Standalone Photovoltaic System: An Adaptive PSO Approach. *Soft Comput.* **2023**, *27*, 8223–8232. [CrossRef]
37. Huang, X.; Li, Q.; Tai, Y.; Chen, Z.; Liu, J.; Shi, J.; Liu, W. Time Series Forecasting for Hourly Photovoltaic Power Using Conditional Generative Adversarial Network and Bi-LSTM. *Energy* **2022**, *246*, 123403. [CrossRef]
38. Elsheikh, A.H.; Sharshir, S.W.; Abd Elaziz, M.; Kabeel, A.E.; Guilan, W.; Haiou, Z. Modeling of Solar Energy Systems Using Artificial Neural Network: A Comprehensive Review. *Sol. Energy* **2019**, *180*, 622–639. [CrossRef]
39. Sidorov, D.; Liu, F.; Sun, Y. Machine Learning for Energy Systems. *Energies* **2020**, *13*, 4708. [CrossRef]